International Journal of Multiphase Flow 35 (2009) 710–724

Contents lists available at ScienceDirect

International Journal of Multiphase Flow

journal homepage: www.elsevier.com/locate/ijmulflow

Investigation of the particle-laden airflow generated by a pseudo-machining operation

Emmanuel Belut [a,1], Francis Bonthoux [b], Benoît Oesterlé [a,*], Jean-Raymond Fontaine [b], Abdelhamid Kheiri [a]

[a] LEMTA, Nancy-University, CNRS, ESSTIN, 2 rue Jean Lamour, 54519 Vandoeuvre-lès-Nancy, France
[b] INRS, avenue de Bourgogne, B.P. 27, 54501 Vandoeuvre-lès-Nancy, France

ARTICLE INFO

Article history:
Received 3 October 2008
Received in revised form 24 March 2009
Accepted 3 April 2009
Available online 12 April 2009

Keywords:
Lagrangian tracking
LES
Machining operation
Particle dispersion
PDPA
PIV

ABSTRACT

A test rig recreating a typical machining induced gas–solid flow is used to investigate the behaviour of the emitted pollutant particles and their effect upon the airflow around the machine tool. The flow is driven by a rotating cylinder and a tangential jet of inertial solid particles. Experimental data concerning both particle flow and air flow are collected by means of phase Doppler particle analyser (PDPA) and particle image velocimetry (PIV). After describing the specific treatments used to discriminate the two phases, complete results are provided and discussed. Additionally, with the main objective being to optimize the design of pollutant capture devices for machining systems, tentative numerical simulations are carried out and compared to experimental data. For the one-phase case (air flow without particles), good agreement between simulations and experiments is found and the superiority of a wall-function based large eddy simulation (LES) over realizable $k-\varepsilon$ modelling is highlighted. For two-phase cases, combination of LES and Lagrangian tracking with two-way coupling leads to simulation results that are reasonably accurate considering the low degree of modelling and the empiricism involved. Particle-to-particle collisions, disregarded in simulations, appear to be a predominant phenomenon in the jet source region, thus partly explaining some discrepancies observed between simulations and experiments.

1. Introduction

Machining, and in particular the hard-metal machining sector, is an important source of employee exposure to inhalable dust carrying a health risk, cobalt being one example. In this respect, INRS (Institut National de Recherche et de Sécurité) is currently involved in developing a method to design pollutant capture devices based on numerical simulation of the two-phase flows (gas/particles) produced by machining systems. The particles of pollutants emitted during machining can generally be divided into two main types: small particles with short response time, presenting a health hazard, that are transported passively by the airflow, and bigger particles, whose health impact is low, but that affect massively the airflow and its turbulence, and hence the dispersion of the small particles. The main issue being to predict numerically the dispersion of these small particles, there is a need for a modelling approach that can accurately predict both turbulent flows generated by rotating pieces and turbulent flows driven by inertial particles.

Most of machining operations involving human operators generate airflows with typical Reynolds number ranging from 10^4 to 10^5 (based on the radius and rotation speed of the revolving element). The transient nature of the machining process, the presence of protruding parts on the rotating element (chuck jaws, teeth), as well as the time evolving geometry, make the existence of a stationary mean flow questionable if not impossible, hence the necessity of using transient simulations. Machining induced airflows are characterized by strong streamlines curvature, rotor–stator interactions, and turbulence occasionally dominated by vortices shed behind protruding parts of rotating elements. These characteristics are known to be unfavourable to RANS modelling. Experiments on three-dimensional turbulent boundary layers (typically encountered against a circular saw) revealed significant misalignment of the Reynolds shear stress vector with respect to the mean velocity gradient vector (Littell and Eaton, 1994; Bradshaw and Terrell, 1969), thus invalidating the concept of scalar eddy viscosity. More recently, while considering the case of a simple rotor–stator flow, Andersson and Lygren (2006) showed numerically that this misalignment could keep up far beyond the buffer region. Therefore isotropic RANS eddy-viscosity models are likely to fail

* Corresponding author. Tel.: +33 383 685080; fax: +33 383 685085.
E-mail addresses: belut@imft.fr (E. Belut), francis.bonthoux@inrs.fr (F. Bonthoux), benoit.oesterle@esstin.uhp-nancy.fr (B. Oesterlé), jeanraymond.fontaine@inrs.fr (J.-R. Fontaine), abdelhamid.kheiri@esstin.uhp-nancy.fr (A. Kheiri).
[1] Present address: IMFT, allée du Professeur Camille Soula, 31400 Toulouse, France.

0301-9322/$ - see front matter © 2009 Elsevier Ltd. All rights reserved.
doi:10.1016/j.ijmultiphaseflow.2009.04.002

partially in rotor–stator flows, and efficient modelling of machining airflows would require, at least, the use of an unsteady RANS model fully taking Reynolds stresses into account. In terms of computational complexity, large eddy simulation (LES) appears to be a competitive alternative, provided that the mesh requirements remain reasonable. This can be achieved by coarsely resolving the LES in the near-wall region, which is the most demanding zone in terms of spatial discretization, and modelling the flow using a wall-function in this region. This introduces quite a lot of empiricism, but can be partly justified in flows in which near wall turbulence is not a main issue. We found, however, that such a wall-function based LES performs surprisingly well for the specific case of the smooth spinning disc, where wall turbulence is fundamental (Belut et al., 2005). Additional evaluation of the performances of such a LES applied to real-like machining conditions can be obtained from comparison with the measurements performed on a test rig that was realized and instrumented to serve as a reference case.

The experimental apparatus and measurement techniques are described in the next Section, then the paper goes on to present the numerical methods used to compute the motion of the gaseous and discrete phases in the test rig. In Section 4, experimental results are given and discussed for both the single-phase airflow and the two-phase cases, and comparison is proposed with the numerical predictions to evaluate the interest of the simulation technique.

2. Experimental facility and measurement techniques

The original experimental apparatus developed, sketched in Fig. 1, has been briefly presented formerly (Belut et al., 2006). It is made up of an aluminum cylinder (diameter 130 mm, length 150 mm) rotating inside a transparent parallelepiped-shaped enclosure (400 × 400 × 600 mm). A particle jet recreating the ventilation effects of a real pollutant is obtained thanks to a feeding system that continuously pushes spherical glass microbeads in a metallic nozzle against the rotating cylinder, whose surface has been made rough in order to help evacuate the particles by friction. The obtained particle jet is stable, and its flow rate is controlled.

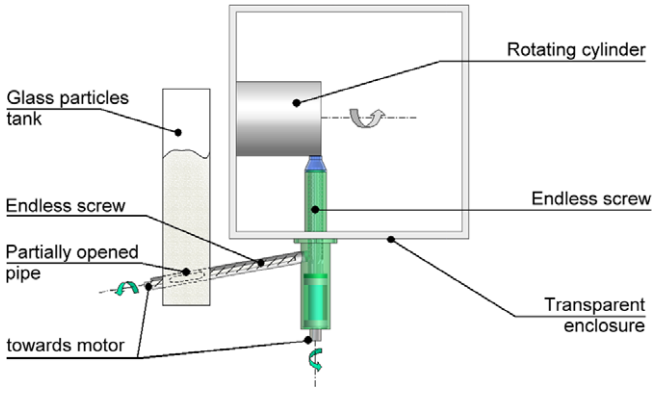

Fig. 1. Test rig and feeding system overview.

2.1. Discrete phase measurements

Particle velocities, diameters, fluxes and concentration in the jet were measured using a phase Doppler particle analyser [PDPA] (Bachalo, 1994), thanks to a Dantec two components PDPA measurement system linked to a Dantec 50 N 10 PDA signal processing unit. The laser source employed was an Argon-Ion Coherent Innova 70-3 laser, the useful wavelengths being 514.5 and 488 nm. Measurements were taken in reflected light, the transmission and reception axes forming an angle of 100° (reflection angle of 80°). Samples of the glass particles employed were characterized beforehand with a Malvern Mastersizer granulometer in order to corroborate the results obtained by PDPA. This operation was repeated regularly during the measurement campaign, as the microbeads were recycled after use, which could have led to granulometric modifications given the abrasion to which particles were subjected in the feeding system. The particle sphericity was also checked in several samples with an optical microscope, as this criterion has a determining impact on the reliability of the granulometric measurements obtained by phase Doppler anemometry. An amount of irregularly shaped particles lower than 3% was certified by the producer, and observations showed that most of sphericity aberrations were in fact particles sticked together by the manufacturing process. The resulting bond between particles appeared to be easily broken during the transit of the particles in the feeding system. All these examinations revealed no significant microbead modification during use.

Two classes of particles were used in the study, namely 50–150 μm and 100–200 μm glass spheres. The diameter distributions can be efficiently modelled by a Rosin–Rammler law with parameters reported in Table 1.

As the equipment used enabled to get only two velocity components, the measurements were performed twice: the third velocity component was obtained through 90° rotation of the test rig between the two sets of measurements. The PDPA measurements focused on the region close to the origin of the jet, the seeding density being too low elsewhere. Two main planes were explored, located 30 mm and 60 mm from the point of emission and oriented normally to the main axis of the jet, as shown in Fig. 2. Additional data points were also taken through the vertical and horizontal planes of symmetry of the jet.

2.2. Gas phase measurements

The particle image velocimetry (PIV) technique was used to characterize the motion of the gas phase in the test rig. Illumination was realized through a frequency doubled Nd:Yag laser emitting 10 ns duration length pulses in 532 nm wavelength. Images were taken by a 12-bit, 1324 × 1024 pixels CCD HiSense MKII camera. Both single phase (i.e., without jet of solid particles) and two-phase measurements were carried out. 5 μm dolomite particles were used for seeding.

Table 1
Summary of test conditions and particle properties.

Cylinder rotation speed (rpm)	Cylinder peripheral speed (ms^{-1})	Particle mass flow rate ($g\,s^{-1}$)	Particle average velocity at 30 mm from injection (% R)	Particle size distribution	Rosin–Rammler median diameter (μm)	Rosin–Rammler spread parameter
500	3.41	1.5 ± 6%	80.1%	100–200 μm	158.5	7.98
1000	6.83	1.5 ± 6%	81.4%	100–200 μm	158.5	7.98
1000	6.83	0.955 ± 6%	68%	50–150 μm	104.5	5.98
1000	6.83	0	–	–	–	–
500	3.41	0	–	–	–	–

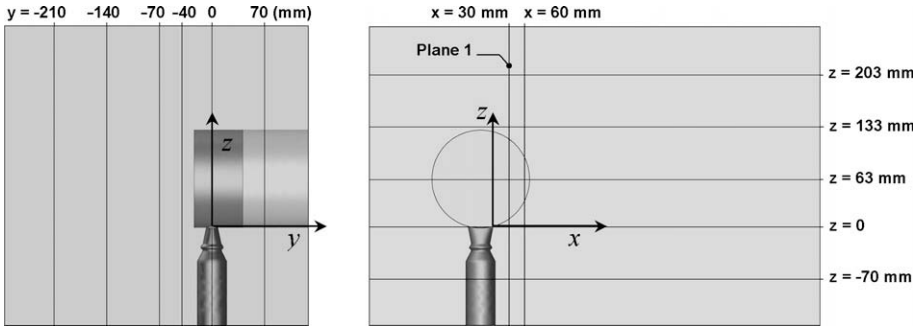

Fig. 2. Measurement planes for PDPA measurements (discrete phase, x = constant) and PIV measurements (gas phase, y = constant and z = constant).

A robust adaptive PIV algorithm employed to compute displacement fields was developed on the basis of the method proposed by Thomas et al. (2005). It uses successively phase correlation as similarity measure to estimate the global displacement field, and normalized cross-correlation as final estimator. The association of the two similarity measures allows an automatic identification of interrogation windows where the local motion cannot be approximated as linear due to strong shear or rotation, in which case the correlation peaks of the two similarity measures are not coincident, hence providing a first validation criterion of the measurement. A second validation criterion is given by the correlation peak height, since the two correlation functions are normalized. Using a Monte–Carlo method, we evaluated the probability that two non-correlated random images present a correlation level greater than a given threshold, as a function of the image size. This makes it possible to define a minimum correlation level to retain a measurement; this level was set so that the probability of obtaining a similar correlation level from random noise was less than 1%. The program was validated using synthetic translation of images (Stanislas et al., 2003; Okamoto et al., 2000) and experimental translation (successive pictures of a black plate seeded with glass particles and subjected to a known translation). The evaluated peak locking error was of 0.036 pixels for the 64 × 64 pixels interrogation windows employed.

2.2.1. Phase discrimination

As both glass particles and seeding particles were visible on the obtained pictures, elimination of the glass particle images was required to give access to the airflow through PIV analysis. The glass particle concentration on the pictures was sufficiently low to make

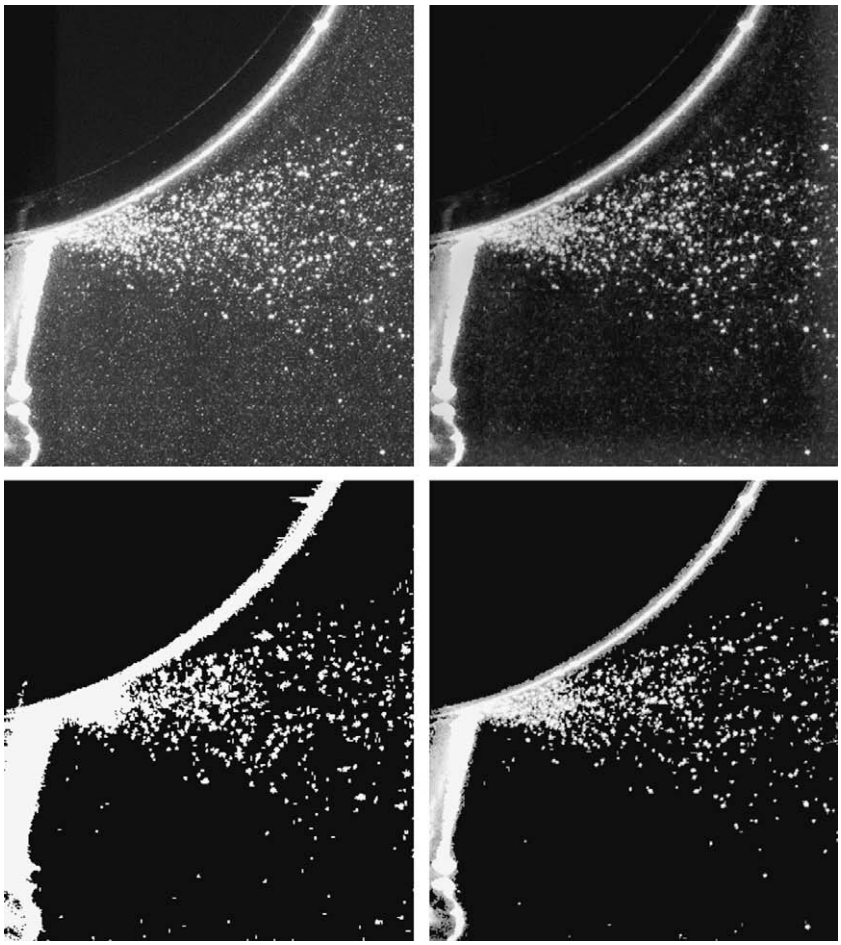

Fig. 3. Phase discrimination procedure: original (top left), erosion (top right), binarization (bottom left), and reconstruction (bottom right).

a morphology-based discrimination feasible, even if a fluorescence based method would have been preferable. The employed discrimination algorithm (Belut, 2006) works in the following way: in a first time, the background of the picture is equilibrated by removing low frequency variation of luminosity. Spots corresponding to glass particles images are then detected on a size criterion, by low-pass filtering through image erosion. Eroding is a fundamental morphological operation that consists in comparing the neighbourhood of all pixels of an image with an elementary feature called structuring element or kernel, and keeping the value of each pixel only if its neighbourhood matches the structural element. As a result, all features of the image are shrinked and features smaller than the structuring element are eliminated. In the present case the structuring element is a square of 2×2 pixels. After this eroding operation, most of the tracer particles are removed from the image, and only laser reflections and glass particles can be seen, however shrinked (Fig. 3, top-right frame). The purpose of the next steps of the algorithm is to reconstruct as exactly as possible the shape of these reflections and glass particles in the original image. The eroded image is thus binarized to obtain a map of "seeds" situating the approximate location of glass particles (binarization consists in reducing the 8-bits grayscale image to a 2-bits black and white image, the threshold above which a pixel is considered white being here of 33% of the maximum of the grayscale). These seeds serve as sources to reconstruct the images of glass particles, thanks to a conditional reconstruction algorithm.

The conditional reconstruction procedure works in the following way: each seed pixel is examined in the original image, and if its gray value is above a given threshold, it is copied in an initially black image. The procedure is then extended recursively to its neighbours, until the growth of seeds stops due to the lack of sufficiently bright neighbouring pixels. At the end of this operation, the pixel values of the new image are identical to the values of the corresponding pixels in the original image provided they can be connected to an original seed by at least one continuous path of sufficiently bright pixels. Hence the original shape of glass particles and reflections is isolated from the background of the image and from the tracer particles of the gas phase. The reconstruction threshold was determined empirically so as to remove all laser reflections in single phase cases: a value such that 95% of the pixels of the image are less bright than this threshold was found to yield satisfactory results.

Any non-black pixels in this reconstructed image must be masked during the PIV treatment, so as not to affect the velocity measurements of the gas phase. This is done by affecting to the pixels to be masked a temporary value during the computation of similarity measures which does not modify the value of the correlation function for any relative displacement of paired interrogation windows. This neutral value is a zero gray level when phase correlation is used, whereas it is the mean gray level of the interrogation window when normalized cross-correlation is employed.

The steps of the discrimination algorithm are illustrated in Fig. 3. The represented area corresponds to the region at the origin of the particle jet, the cylinder and injection nozzle being clearly visible thanks to laser light reflections.

2.2.2. Particle masking efficiency

As in some cases glass particle images may appear of the same size as tracer particles, for instance when they are at the edge of the laser sheet, a bias in the phase discrimination procedure can be expected. Hence a purely size-based phase discrimination cannot be totally effective. It should be noted, however, that in our case the concentration of glass particles is quite low, except in the jet source region. Thus, glass particle images generally contribute only to the background noise of cross-correlation functions. In the jet source region, where the concentration of glass particles is high, these particles present a significant slip velocity with respect to the fluid, which makes their presence in paired interrogation windows of two successive PIV images unlikely, the time interval between two successive shots being adjusted for the velocity field of the fluid. Hence, in that case also, glass particle images generally add noise to cross-correlation functions.

Evaluation of the masking algorithm can be obtained by analysing synthetic images of a two-phase flow (Belut, 2006). This was done simply by adding to a pair of PIV images, for which the displacement is known, a pair of images of larger particles subjected to another displacement. The application of the phase discriminating PIV algorithm to such synthetic images indicated a discrimination error on seeding particle displacement lower than 1.4×10^{-2} pixels when 20% of the image area was covered with large particles, and lower than 7.8×10^{-3} pixels when less than 5% of the image area consisted in large particles. Except in the jet source region, less than 5% of the PIV pictures were covered with glass particle images, which yielded a typical bias error on the fluid velocity equal to 0.03% of the cylinder peripheral velocity $R\omega$ when glass particles were present (R being the cylinder radius and ω its angular velocity). However, this evaluation does not consider the possibility for a glass particle to appear on the PIV images as a spot of size comparable to the tracer particle size, a drawback which could not be avoided. Hence the real phase discrimination error was probably higher, and measurement results obtained for the carrier phase in the source region of the jet of particle could not be considered as absolutely reliable.

2.3. Experimental configurations and measurement uncertainties

Parameters such as the cylinder rotational velocity, the particle flow rate and granulometry were varied to provide different experimental configurations. The properties of the various configurations are summarized in Table 1.

The airflow in the test rig was characterized by carrying out measurements in six vertical planes parallel to the front face of the cylinder (y = constant) and five horizontal planes (z = constant), located as shown by Fig. 2. As lighting conditions did not allow the acquisition of a full plane in a single shot, each plane was divided into 8 frames, overlapping by 22%. The reconstruction of a full measurement plane from these 8 frames introduced some slight location uncertainty always lower than 4 pixels, that is 0.68 mm.

The peak locking error of the PIV algorithm induced an uncertainty of $8\ \mathrm{mm\ s^{-1}}$ on the instantaneous air velocity at $\omega = 1000$ rpm, and of $4\ \mathrm{mm\ s^{-1}}$ at $\omega = 500$ rpm, this error being without any effect on the mean velocities as pointed out by Christensen (2004). Each frame of each measurement plane was shot 300 times for single phase cases and 150 times for two-phase cases, which led to a statistical uncertainty on mean velocities lower than $0.2\%\ R\omega$ for single phase cases and $0.4\%\ R\omega$ for two-phase cases. Thanks to frame overlapping, the number of velocity samples was doubled for 20% of the measurement points and multiplied by four for 2% of them. The time interval between image pairs was chosen such that successive velocity fields were uncorrelated.

The interrogation windows used here, of 64×64 pixels with 50% overlap, resulted in a resolution of one vector every 5.4 mm, that is 8000 vectors per measurement plane.

3. Numerical methods

3.1. Gas phase

The airflow generated by the test rig was fully turbulent and could be considered isothermal and incompressible under the

experimental conditions. The finite volume approximation was used to solve the equations of motion for the fluid. Two approaches were employed to model the turbulence of the airflow, namely the realizable $k-\varepsilon$ model by Shih et al. (1995) with standard wall functions (for single phase cases only), and, on the other hand, large eddy simulation (LES) relying on the subgrid scale (SGS) model by Kim and Menon (1997). In this model, SGS stresses are classically modelled according to a subgrid turbulent viscosity hypothesis:

$$\tau_{ij} - \frac{2}{3}\rho k_{sgs}\delta_{ij} = -\rho \nu_t \left(\frac{\partial \overline{u}_i}{\partial x_j} + \frac{\partial \overline{u}_j}{\partial x_i}\right) \quad (1)$$

where ρ and $\overline{\mathbf{u}}$ denote the fluid density and mean velocity, respectively, and x_i are Cartesian coordinates. The subgrid turbulent viscosity ν_t is expressed in terms of the cell volume V by

$$\nu_t = C_k\, k_{sgs}^{1/2}\, V^{1/3} \quad (2)$$

and the SGS kinetic energy k_{sgs} is obtained through its transport equation:

$$\frac{\partial k_{sgs}}{\partial t} + \frac{\partial \overline{u}_j k_{sgs}}{\partial x_j} = -\frac{\tau_{ij}}{\rho}\frac{\partial \overline{u}_i}{\partial x_j} - C_\varepsilon \frac{k_{sgs}^{3/2}}{\Delta} + \frac{\partial}{\partial x_j}\left(\nu_t \frac{\partial k_{sgs}}{\partial x_j}\right) \quad (3)$$

where Δ is the local filter width. The coefficients C_k and C_ε are computed dynamically (Kim and Menon, 1997; Kim, 2004). For finite volume discretization, the local filter width depends explicitly on the cell volume (i.e., $\Delta = V^{1/3}$).

The governing equations were discretized on an unstructured tetrahedral grid, which allowed precise control of the local grid size, and hence of the LES filter width distribution. A central differencing scheme was used for the convective terms of the momentum equations, together with an implicit second-order time advancement scheme.

To ensure the SGS model consistency, the computational grid was built in order to obtain a local cell size equal to the Taylor microscale $\lambda = \sqrt{10\nu k/\varepsilon}$, estimated from a preliminary k–ε computation (ν, k, ε are the fluid kinematic viscosity, the turbulent kinetic energy and its dissipation rate, respectively). At the wall, a sufficiently resolved LES would require a grid spacing (in wall units) such that $\Delta y^+ \approx 1, \Delta x^+ \approx 100$ and $\Delta z^+ \approx 20$, y being the wall normal direction and x the mean flow direction (Piomelli, 2004). This requirement could be satisfied on the surrounding walls of the test rig, where the flow velocity was moderate, without dramatic increase of the computational cost. On these walls, a structured boundary-layer type mesh was then built, made up of ten layers of cells with geometrically increasing thickness, located between $y^+ = 1$ and $y^+ = 60$ (with $\Delta x^+ \approx \Delta z^+ \approx 50$). A no-slip boundary condition was then used for such walls. Regarding the rotating cylinder wall, fully resolving the near wall region would have been computationally too demanding. The first grid points were therefore located at $y^+ \approx 30$, and the standard wall function was used as boundary condition. However, in order to allow for the cylinder surface roughness, whose dimensionless height is $\epsilon^+ \approx 7$ at 500 rpm and $\epsilon^+ \approx 13$ at 1000 rpm, the wall shear stress was prescribed according to the experimental correlation proposed by Theodorsen and Regier (1944) in terms of the roughness height. This approach, which introduced some empiricism especially considering that, besides particles, the rotation of the cylinder is the only source of momentum in the test rig, was expected to yield a correct overall momentum transfer between the rotating cylinder and the fluid in spite of the crude modelling of the boundary layer. The near cylinder zone was the only insufficiently resolved region of the simulation. The resulting grid consisted in 9×10^5 cells at 500 rpm and 1×10^6 at 1000 rpm. From examination of the predicted residual kinetic energy, it appeared that the maximum value of k_{sgs}, which occurs in the near cylinder region, was about 12% of the total turbulent kinetic energy at both rotation speeds.

For the realizable $k-\varepsilon$ computations (single phase cases only), the computational grid was the same as for LES except close to the surrounding walls where standard wall functions were used ($y^+ \approx 60$ for the first grid points).

3.2. Discrete phase

The motion of the glass particles emitted by the test rig was modelled using a Lagrangian approach and two-way coupling with the gas flow equations.

3.2.1. Initial conditions for the discrete phase

The particle injection properties were deduced from the PDPA measurements in taking into account the granulometry and the spatial distribution of particle concentration and velocities at injection. As particle data could not be collected at a distance closer than 30 mm from the jet source, the actual injection properties were unknown. Therefore the initial conditions for particle trajectory computations were set so as to retrieve in the simulations the particle properties that were measured at 30 mm from the jet source. This was achieved by means of a prediction–correction algorithm lying on the assumption of quasi-rectilinear motion of the particles between their starting location and the first PDPA measurement plane (further referenced as "plane 1", see Fig. 2), which crosses normally the particle jet at 30 mm from its origin. This hypothesis was satisfied in practice provided that no inter-particle collisions occur: given the geometry, it could be assumed that the particle initial slip velocity was at most comparable to $R\omega$, from which we could evaluate an initial particle Reynolds number $Re_{p_{init}} = R\omega d_p/\nu$ (d_p denoting the particle diameter) and a typical initial particle response time $\tau_{p_{init}}$:

$$\tau_{p_{init}} = \frac{\tau_p}{f_{init}} = \frac{1}{f_{init}}\frac{\rho_p d_p^2}{18\rho\nu} \quad (4)$$

where τ_p is the Stokes response time and f_{init} is the correction factor for finite Reynolds number, $f_{init} = C_D/(24/Re_{p_{init}})$, the drag coefficient C_D being estimated in terms of $Re_{p_{init}}$ as mentioned in Section 3.2.3 below.

From this initial particle response time, a typical response length L_p along which the particle motion is governed mainly by the initial conditions was assessed by $L_p = R\omega\tau_{p_{init}}$, assuming a particle initial velocity equal to $R\omega$. Table 2 reports the corresponding initial response lengths obtained for the studied configurations, based on the particle characteristic diameter $d_{p_{95}}$ (defined so that 95% of the total mass are made up of particles having a diameter greater than $d_{p_{95}}$). The values of these response lengths confirm that the fluid had only a weak effect on the particle trajectories along the first 30 mm separating the initial location of particles from plane 1. Thus, to estimate the particle injection properties (velocity $\mathbf{u}_p$ and position) from particle data collected in plane 1, their equation of motion was approximated by:

$$\frac{d\mathbf{u}_p}{dt} = -\frac{f}{\tau_p}\mathbf{u}_p + \mathbf{G}, \quad (5)$$

Table 2
Typical response length of particles.

Particle size distribution	Cylinder peripheral speed ($m\,s^{-1}$)	Particle diameter d_{p95} (μm)	Particle response length (mm)
100–200 μm	3.41	109	136
100–200 μm	6.83	109	204
50–150 μm	6.83	64	90

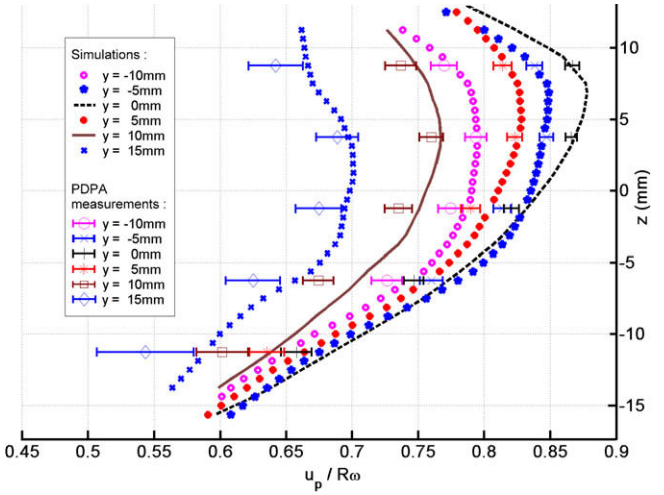

Fig. 4. Particle axial (x-direction) mean velocity in plane 1.

f being still the drag correction factor, i.e., $f = C_D/(24/Re_p)$ with $Re_p = |\mathbf{u}_p|d_p/\nu$, and $\mathbf{G}$ being an unknown constant term acting along the particle trajectory. Such a procedure amounts to model the effects of non-negligible (but unknown) fluid velocity through a constant acceleration added to gravity. Using this elementary model and a simple simulation of the test rig (through realizable k–ε modelling and neglecting particle/turbulence interactions), an iterative algorithm provided particle initial conditions leading to the desired particle flow properties in plane 1, as measured by PDPA. To ensure that the simulated particles present the same properties as the measured particles in plane 1, the convergence criterion was set to 0.5 mm for positions and to 1×10^{-3} m s^{-1} for velocity components. One iteration of the algorithm was generally sufficient to reach this level of convergence. The estimate of the equivalent acceleration $\mathbf{G}$ acting along a particle trajectory was computed iteratively. For given injection conditions $(\mathbf{u}_{p0}, x_{p0})$ and the obtained properties in plane 1 $(\mathbf{u}_{p1}, \mathbf{x}_{p1})$, the convergence criterion on $\mathbf{G}$ was such that the velocities and positions $(\mathbf{u}'_{p1}, \mathbf{x}'_{p1})$ obtained by integrating Eq. (5) differ by less than 0.1 mm and 1×10^{-4} m s^{-1} from the target properties $(\mathbf{u}_{p1}, \mathbf{x}_{p1})$.

3.2.2. Efficiency of the algorithm

A validation step was incorporated into the algorithm to ensure that the initial conditions obtained for each particle are geometrically possible, i.e., the starting location of the particle is inside the simulated domain. This validation step eliminates the particles whose velocity and position in plane 1 cannot be explained by assuming a quasi-rectilinear motion between the jet source and plane 1. This means that the injection conditions used for the simulations cannot reproduce the exact velocity distribution measured in plane 1. As a consequence, even if the predicted particle mean velocity profiles in plane 1 are in good agreement with the experiments, as shown by Fig. 4, the particle fluctuating velocities in plane 1 are underestimated since the extreme values of the velocity distributions can generally not be explained by a quasi-rectilinear motion emanating from the jet source. With the initial conditions provided by the algorithm, the particle r.m.s. velocity obtained in plane 1 reaches, on average, 68% of its target (experimental) value. As the assumption of quasi-rectilinear motion of particles between their injection and plane 1 is valid provided that the particles interact only with the fluid, it is extremely probable that the particles for which such linear motion is geometrically impossible underwent one or several collisions, either with the cylinder or with other particles, as will be discussed later on.

3.2.3. Particle equation of motion

In the considered case in which $\rho_p \gg \rho$, the added mass force, history force and pressure gradient force can be neglected. Also neglecting other hydrodynamical effects such as Magnus and Saffman lift, the equation of motion used to integrate particle trajectories reduces to:

$$\frac{d\mathbf{u}_p}{dt} = \frac{3}{4}\frac{\rho}{\rho_p}\frac{C_D}{d_p}(\bar{\mathbf{u}} - \mathbf{u}_p) + \mathbf{g} \tag{6}$$

where $\bar{\mathbf{u}}$ is the resolved instantaneous fluid velocity, and $\mathbf{g}$ denotes gravitational acceleration. The drag coefficient C_D was expressed using the correlation of Morsi and Alexander (1972). Inter-particle collisions were also neglected during trajectory calculation, despite their possible importance in the jet source region as discussed later in Section 4.3.

3.3. Coupling between phases

3.3.1. Interaction between particles and resolved scales

Whereas the dispersive effect of the resolved turbulent scales upon particles is predicted by Eq. (6), it must be kept in mind that the gas flow may be affected by the discrete phase motion, i.e., two-way coupling must be considered. This was achieved by introducing a source term $\mathbf{f}_v$ in the momentum equations of the fluid flow, corresponding to the momentum acquired by the fluid from the particles. For a given cell of the finite volume discretization, this source term can be expressed by:

$$\mathbf{f}_v = -\frac{1}{V}\sum_{\text{particle } i \text{ in cell}} \rho_p \frac{\pi}{6} d_{p_i}^3 \left(\frac{d\mathbf{u}_{p_i}}{dt} - \mathbf{g}\right). \tag{7}$$

Hence two-way coupling between the particles and the resolved scales of the fluid motion was fully taken into account.

3.3.2. Interaction between particles and subgrid scales

The influence of subgrid turbulence scales on particle motion was neglected in the simulations, considering their long response time and thus some unresponsiveness to the subgrid scales. More precisely, assuming that the correlation time scale T_{sgs} of the subgrid fluid velocity along the particle path is of the same order of magnitude as the eddy turnover time of the subgrid scales, we can follow Fukagata (2000) to estimate T_{sgs} as:

$$T_{sgs} \approx 0.37\frac{\Delta}{\sqrt{k_{sgs}}} \tag{8}$$

where $\Delta = V^{1/3}$ is the local filter width. From our simulation results, *a posteriori* estimations of T_{sgs} in the domain were obtained using Eq. (8), showing that the ratio τ_p/T_{sgs} exceeds 4 everywhere. This observation consolidates our assumption of negligible influence of the subgrid turbulent fluctuations on the particle motion.

As the way the particles modify the energy transfer from large scales to subgrid scales is not fully understood, the influence of particles on subgrid scales was not taken into account here. Still following Fukagata (2000), however, we can estimate *a posteriori* the particle induced modification of the subgrid turbulent viscosity ν_t using:

$$\nu_t = \nu_t^0\left(1 + \frac{5C_0^{3/2}}{\pi}\frac{\alpha_p\frac{\rho_p}{\rho}}{1 + \frac{\tau_p}{T_L}}\right)^{1/3} \tag{9}$$

where C_0 is the Kolmogorov constant and ν_t^0 is the subgrid turbulent viscosity when no particles are present. This estimation predicts that ν_t can be modified by more than 10% in the most concentrated region of the jet of particles, which suggests that the influence of particles on subgrid scales should have preferably been taken into account in the jet source region.

4. Results and discussion

4.1. Single phase cases

The rotating cylinder tends to act like a centrifugal pump, dragging air along its axis while accelerating it into a rotating motion with radial ejection owing to centrifugal acceleration. The air is then recycled along the walls of the test rig enclosure. The overall airflow is quite complex, presenting multiple recirculating regions due to the geometry of the device.

In Figs. 5 and 6, the mean velocity fields computed by LES as well as by realizable k–ε simulation are compared to the measured field for a single phase case (i.e., no jet of particles, cylinder rotating at 1000 rpm), in the vertical plane crossing the test rig at $y = 0$ (Fig. 5) and in the horizontal plane located at $z = 0$ (Fig. 6). Contour plots of in-plane velocity magnitude are drawn, with figures indicating the lower bound of the velocity magnitude in each region, expressed in percent of the cylinder peripheral velocity $R\omega$. Such comparisons between experimental and simulated results exemplify qualitatively how LES, even if insufficiently resolved spatially, provides more accurate predictions, in the present case, than a classical eddy viscosity turbulence model. This can be explained by the strong streamline curvature and the turbulence anisotropy, which are known to be particularly unfavourable to eddy viscosity based RANS models. The anisotropy of the turbulence, a feature

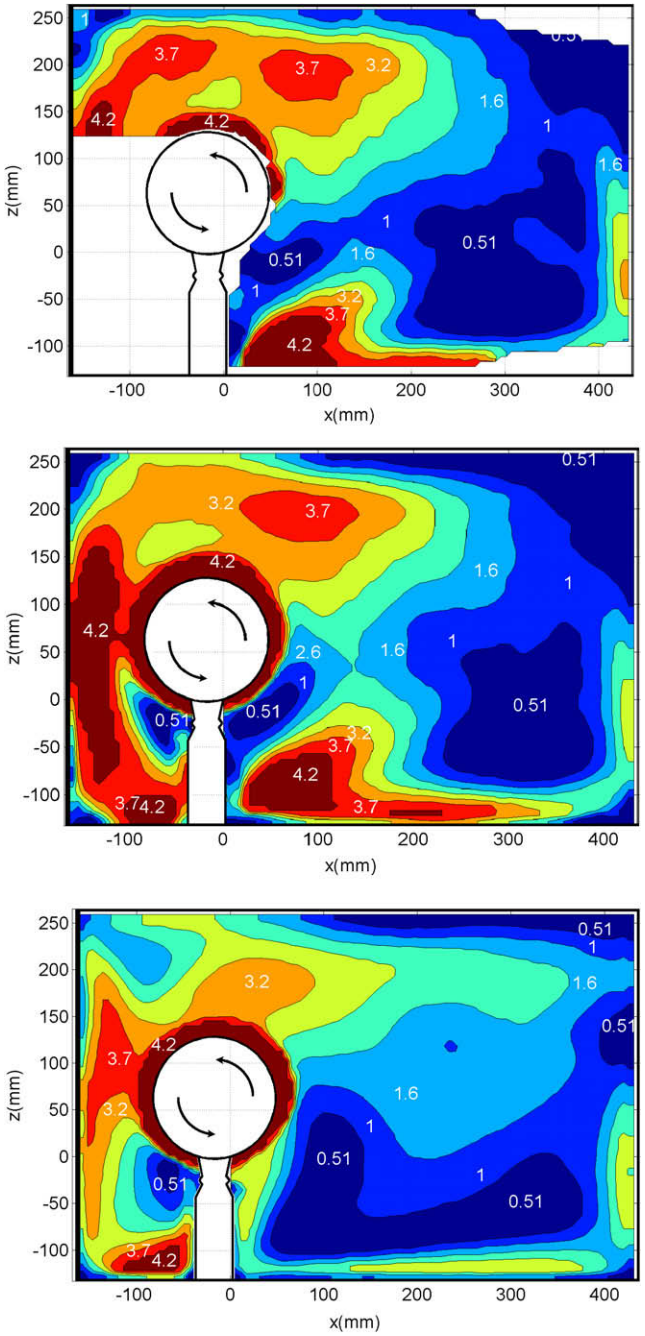

Fig. 5. Contours of mean velocity magnitude in single phase flow in the vertical plane $y = 0$: PIV measurements (top), LES computation (middle) and realizable k–ε computation (bottom).

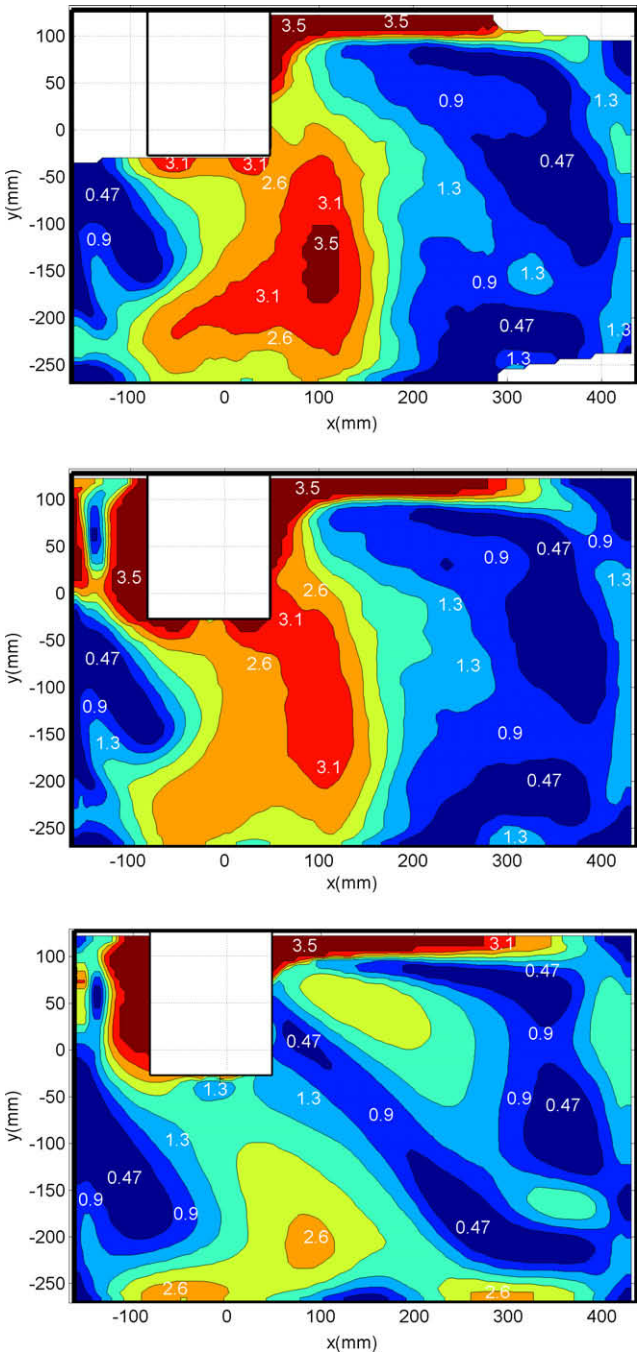

Fig. 6. Contours of mean velocity magnitude in single phase flow in the horizontal plane $z = 0$: PIV measurements (top), LES computation (middle) and realizable k–ε computation (bottom).

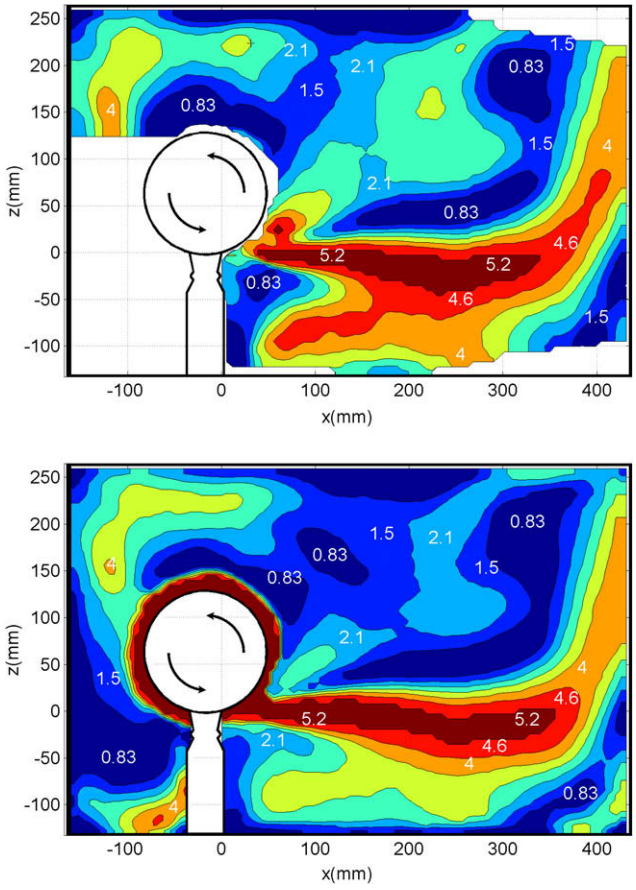

Fig. 7. Contours of mean velocity magnitude of air in two-phase flow in the vertical plane $y = 0$, for $\omega = 1000$ rpm: PIV measurements (top), LES computation (bottom).

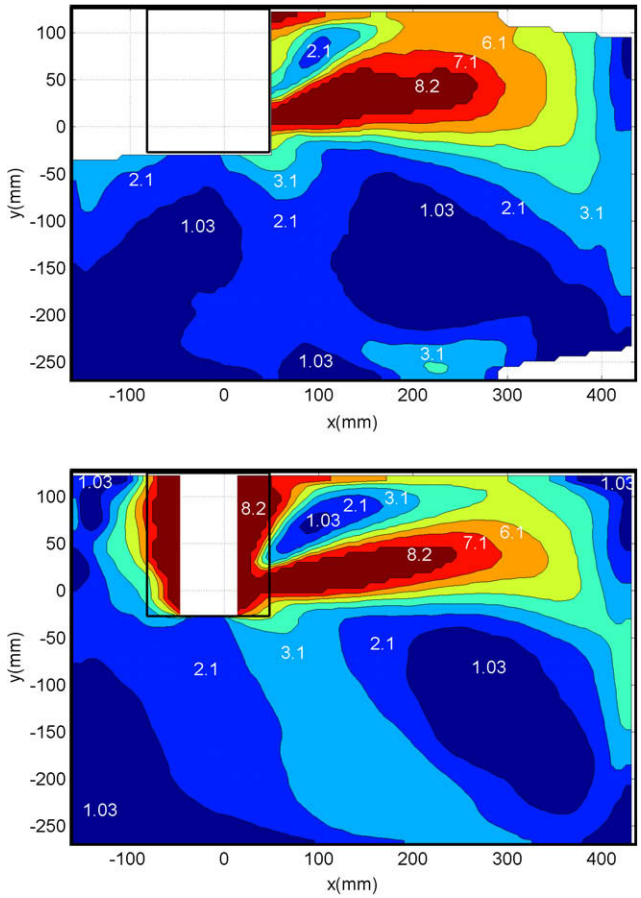

Fig. 8. Contours of mean velocity magnitude of air in two-phase flow in the horizontal plane $z = 0$, for $\omega = 1000$ rpm: PIV measurements (top), LES computation (bottom).

frequently mentioned for rotor–stator flows (Andersson and Lygren, 2006), was clearly observed in our test rig through the PIV measurements of the r.m.s. velocity components (not shown). Such an observation underlines the need for advanced turbulence models in the wider area of rotating machinery induced flows.

4.2. Two-phase cases

4.2.1. Gas phase flow

For two-phase cases, the airflow is driven simultaneously by the rotation of the cylinder and by the jet of glass particles.

Examples of measured and computed mean velocity fields of air laden with 100–200 μm particles are compared in Figs. 7–9, which display the contours of mean velocity magnitude in the vertical plane $y = 0$ for $\omega = 1000$ rpm (Fig. 7) and in the horizontal plane $z = 0$ for $\omega = 1000$ rpm (Fig. 8) and for $\omega = 500$ rpm (Fig. 9). As regards the simulation results, only LES is evaluated here. The overall structure of the mean airflow appears to be reasonably well predicted by the simulations, even if the velocity fields do not match extremely closely. It should be noted that the involved velocities are two order of magnitude smaller than the cylinder peripheral velocity, and that small changes of position generally resulted in significant changes in velocity field due to the rapid spatial variations of the flow, which renders a plane to plane comparison questionable. The horizontal expansion rate of the particle driven air jet can be observed to be slightly underestimated by simulations at 1000 rpm, while at 500 rpm the extremity of the air jet appears to be more deflected from the back wall (supporting the cylinder) than what is found in simulations.

As Figs. 7–9 only provide large scale qualitative comparison between measurements and numerical simulations, examples of detailed mean and r.m.s. velocity profiles for air in the jet of particles are given in Fig. 10 (mean velocity) and Fig. 11 (fluctuating velocity). Velocities are still expressed in percent of the cylinder peripheral velocity, and error bars correspond to 95% confidence interval. In the core region of the jet, air is accelerated by particles, which results in a compensatory inflow coming from outer region of the jet. Close to the cylinder, air is accelerated in the opposite direction by the rotation of the cylinder, and is therefore submitted to intense shear. Unfortunately, due to strong light reflection satisfactory resolution of PIV measurements in this zone could not be achieved. It should also be noticed that the turbulent boundary layer thickness at the cylinder wall at such rotation speeds is comparable to the size of the interrogation windows used for PIV, hence the boundary layer was not resolved at all by our measurements.

Regarding the fluctuating velocities of the gas phase, comparison is not straightforward because velocity fluctuations are filtered out spatially and temporally by both PIV and LES: PIV filtering depends, among other, upon the interrogation window size, upon the homogeneity of the flow and of the tracer distribution, and upon the shooting interval, while LES filtering depends explicitly on the local cell volume and on the related time-advancement step. The velocity fluctuations evaluated experimentally and numerically are therefore underestimated and filtered on a different basis, which makes their comparison questionable. Considering however that most of the fluctuations are due to large eddies which are

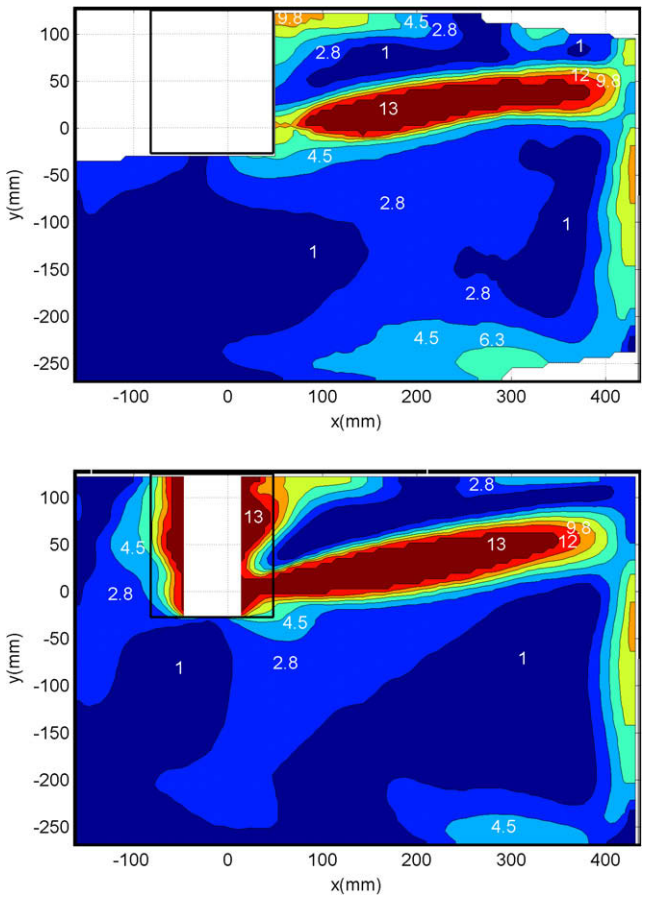

Fig. 9. Same caption as Fig. 8, except $\omega = 500$ rpm: PIV measurements (top), LES computation (bottom).

taken into account by both PIV and LES, the examples of measured and simulated RMS velocity profiles reported in Fig. 11 (1000 rpm case with 100–200 μm particles) show that the level of the numerically predicted fluid fluctuations is in good accordance with the level of measured fluctuations, as far as the two quantities can be compared considering their different nature and statistical uncertainties. Further experimental investigations seem to be needed to conclude definitely on that matter.

4.2.2. Discrete phase flow

Particle mean velocity profiles obtained for ω = 1000 rpm and d_p = 100–200 μm are displayed in Figs. 12 and 13, in which velocities are still expressed in percent of the cylinder peripheral velocity, and error bars corresponding to 95% confidence interval are set for each measurement point. Measured and simulated profiles can be observed to be close to one another, even if the agreement decreases as the distance separating the profile section from the jet source increases. This could be expected considering that differences existing between the predicted and the simulated airflow affect only slightly the particle motion at distances shorter than their typical response length, which is about 200 mm in this case (see Table 2).

As regards the particle fluctuating motion, measured and computed profiles of r.m.s. velocities in directions x and y are shown in Fig. 14 in the same flow case. Close to the jet source, the predicted fluctuations can be seen to be significantly smaller compared to experimental values: this is clearly a remnant of the particle initial conditions used for the simulations, for which velocity fluctuations are underestimated by construction as was pointed out above in Section 3.2.2. As the distance from the jet source increases, particle velocity fluctuations in the y and z (not shown here) direction decrease both in simulations and experiments. By contrast, the simulated particle fluctuating velocity in the main direction of the jet (x) increases slightly with the distance from the jet source, while the measured fluctuations decrease imperceptibly, so that simulation results finally catch up with measurements. This difference of behaviour could be explained by considering the differential deceleration of particles in the x-direction caused by the spread of the particle size distribution. In this direction, the particle slip velocity is maximum and so is particle drag. Given their difference in response time, the smallest particles are then already slowed down while the largest particles remain hardly affected, and hence the spread of the particle velocity distribution is expected to increase. This would be true if only fluid–particle interactions were influent, which is the case in simulations. In practice, however, particle-to-particle collisions are influential and tend to oppose themselves to such an increase of particle fluctuating velocities by increasing the spread rate of the particle jet, by transferring particle translation kinetic energy to rotational kinetic energy, and by making the particle velocity fluctuations more isotropic. On the whole, one can nevertheless observe that acceptable agreement is found between measurements and simulations regarding the particle fluctuating motion.

4.3. Discussion on inter-particle collisions

It has been widely observed in two-phase flows that inter-particle collisions may have a major effect on particle mean velocity and concentration profiles, even for dilute laden flows in which the particle volume fraction does not exceed 10^{-4} (Tanaka and Tsuji, 1991; Oesterlé and Petitjean, 1993; Kulick et al., 1994; Sommerfeld, 1995; Yamamoto et al., 2001). To assess the particle volume fraction in our experiments, one can coarsely consider the particle source as being a rectangle of 16×2.5 mm, i.e., of area $S = 40$ mm^2; assuming that the particle initial velocity is close to the cylinder peripheral velocity $R\omega$, and given the particle mass flow rate q_m, the initial particle volume fraction at the jet source can be approximated by $\alpha_{p_0} = q_m/(\rho_p R\omega S)$. Depending on the studied configurations, α_{p_0} thus varies within the range 1.4×10^{-3} to 4.4×10^{-3}, which already suggests some noticeable influence of particle collisions. If we now assume that the motion of distinct particles is uncorrelated and that their velocity fluctuations are isotropic (with standard deviation σ_p), we can follow Abrahamson (1975) to estimate the mean intercollision time τ_c for particles:

$$\tau_c = \frac{\sqrt{\pi} d_p}{24 \alpha_p \sigma_p}. \tag{10}$$

As the behaviour of the dispersed phase is known to be significantly affected by inter-particle collisions for $\tau_p/\tau_c > 1$ (Crowe et al., 1998; Sommerfeld, 2001; Chagras et al., 2005), it is interesting to assess the particle response time in the jet source region and to compare it to τ_c. In the most favourable cases, the particle initial slip velocity is equal to their ejection speed, that is $R\omega$, and thus the shortest possible initial particle response time $\tau_{p_{init}}$ is given by Eq. 4: assuming that the initial value of σ_p is close to the particle r.m.s. velocity measured at 30 mm from the jet source, i.e., $\sigma_p \approx 0.15\, R\omega$, we obtain a lower bound for the ratio $\tau_{p_{init}}/\tau_c$ at the jet source within the range 4–15, depending on the considered configuration. From this ratio we can conclude that particle-to-particle collisions predominate over aerodynamical effects in the source region of the jet.

Experimental data show that particle-to-particle collisions remain influential at some distance from the jet source, as can be seen in Fig. 15 which displays measurements of the ratio

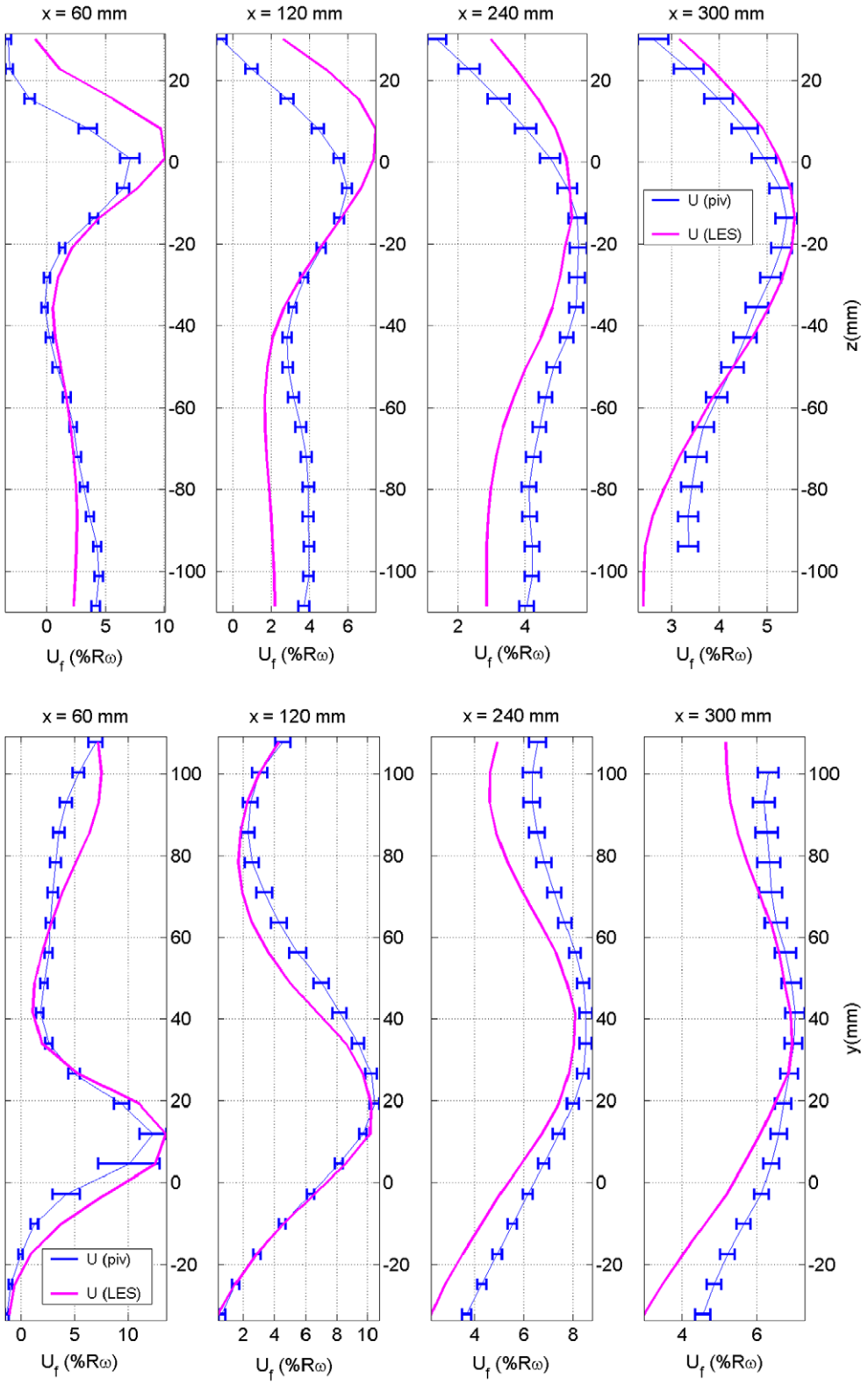

Fig. 10. Air velocity profiles in two-phase flow: comparison between PIV measurements (light lines with error bars) and LES computation (thick lines) for the x-component of mean velocity in the vertical plane $y = 0$ (top) and in the horizontal plane $z = 0$ (bottom).

τ_p/τ_c in the jet cross-section located at $x = 30$ mm. Similar measurements made at 60 mm from the jet source led to $\tau_p/\tau_c \approx 0.3$ in the core region of the jet, showing that the effect of inter-particle collisions might be neglected beyond this distance.

Disregarding particle-to-particle collisions in the numerical simulations is therefore an important source of error in reproducing the particle behaviour in the initial region of the jet, where such collisions transfer translation kinetic energy to rotational energy, which deeply affects the velocity distribution of particles and results in high speed rotation motion of particles. Moreover, hydrodynamical forces such as Magnus lift may even no longer be negligible in this region.

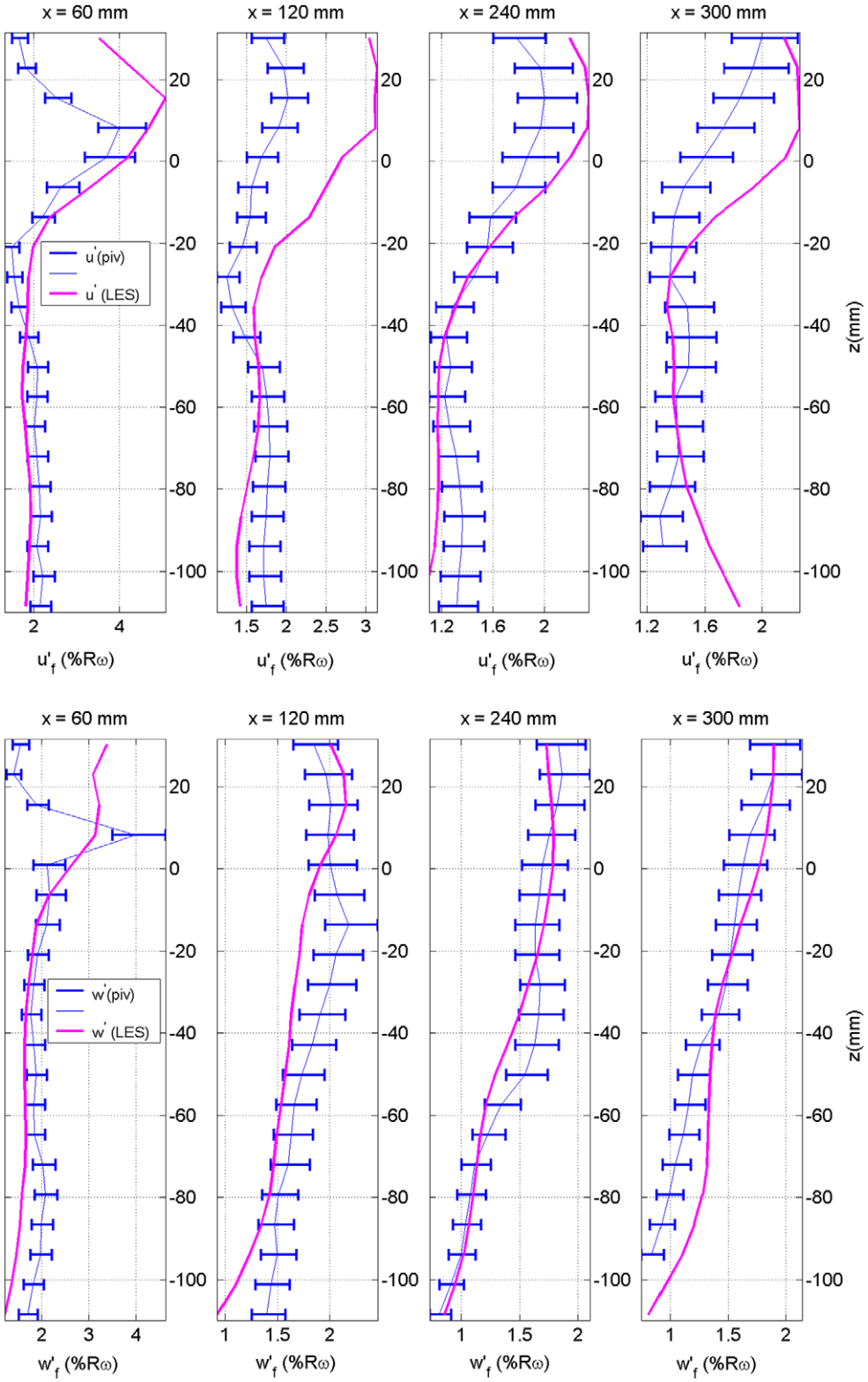

Fig. 11. Fluctuating velocity profiles of air in two-phase flow in the vertical plane $y = 0$: comparison between PIV measurements (light lines with error bars) and LES computation (thick lines) for the r.m.s. velocity in direction x (top) and in direction z (bottom).

5. Concluding remarks

A gas–particle flow representative of machining induced two-phase flows was investigated both experimentally and numerically. The flow was driven simultaneously by a rotating piece and by a highly inertial jet of glass particles. Experiments were carried out using PIV for the gas phase and PDPA for the dispersed phase, while numerical predictions were achieved by means of an Eulerian–Lagrangian approach with two-way coupling.

As could be expected, a standard eddy-viscosity turbulence model such as realizable k—ε was shown to perform poorly even in predicting the airflow in the single phase case. This can be ex-

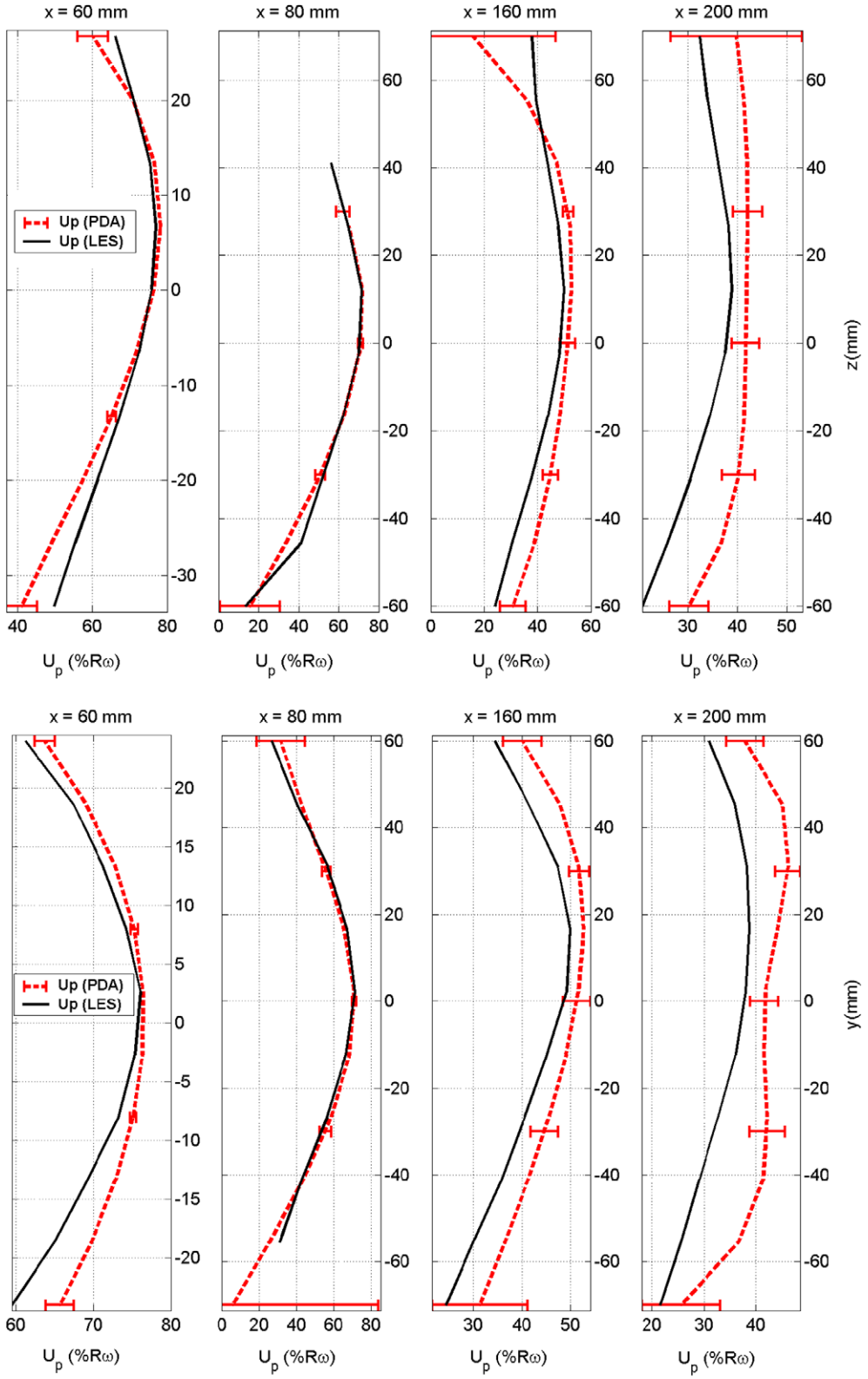

Fig. 12. Particle velocity profiles: comparison between PDPA measurements (dashed lines with error bars) and LES computation (solid lines) for the axial (x-component) mean velocity in the vertical plane $y = 0$ (top) and in the horizontal plane $z = 0$ (bottom).

plained by the highly swirling aspect of the flow and by the inability of eddy-viscosity RANS models to handle the turbulence anisotropy which was observed through PIV measurements of velocity fluctuations. Therefore a LES modelling approach, however based on a wall function near the cylinder wall to be workable in an industrial context, was chosen for the Eulerian prediction of the airflow, providing better results despite the empiricism involved in the low degree of modelling.

Concerning the two-phase case, the advantage of using LES instead of RANS modelling lies mainly in the implicit coupling be-

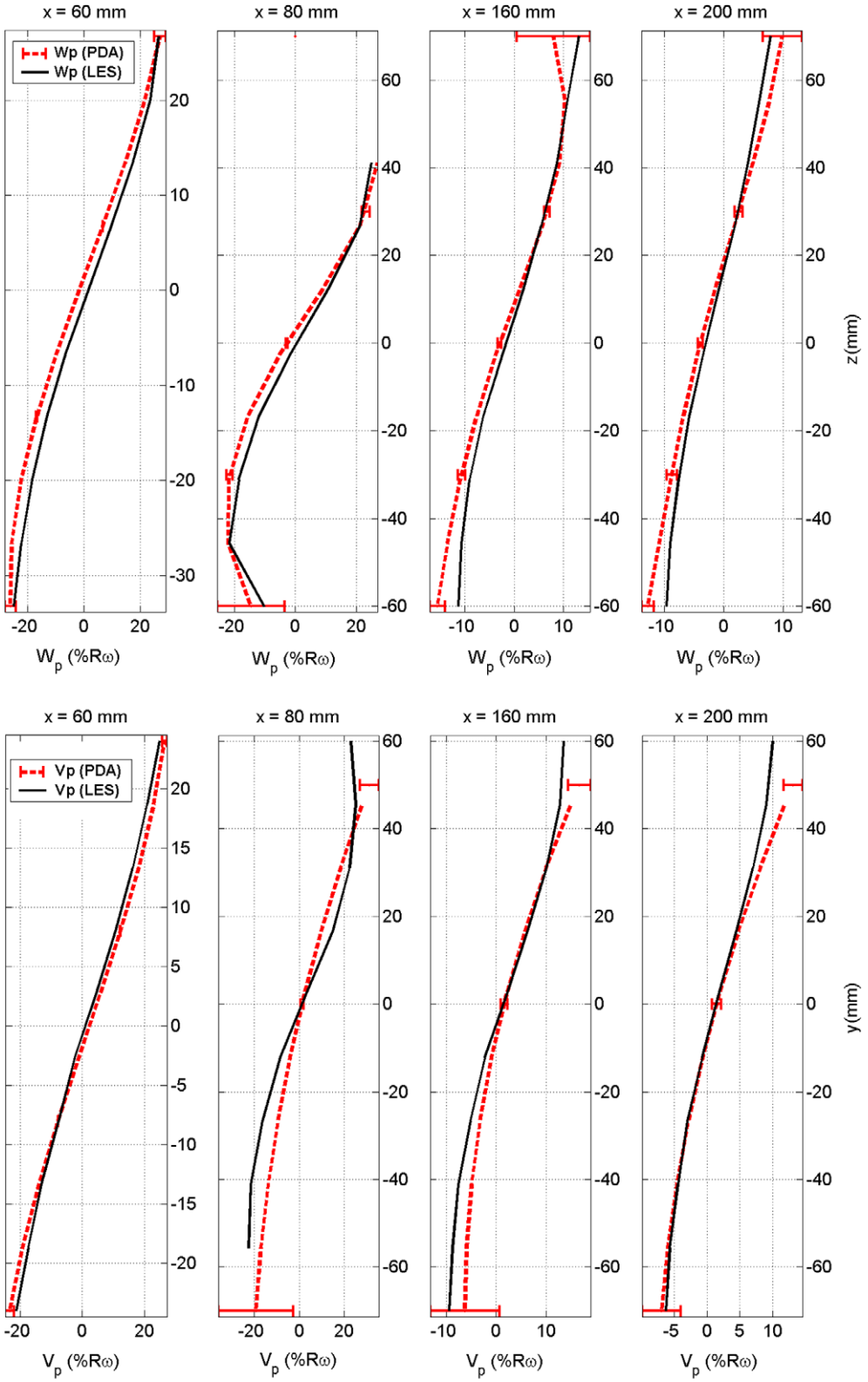

Fig. 13. Particle velocity profiles: comparison between PDPA measurements (dashed lines with error bars) and LES computation (solid lines) for the vertical (z-component) mean velocity in the vertical plane $y = 0$ (top) and for the y-component of mean velocity in the horizontal plane $z = 0$ (bottom).

tween the particles and the resolved scales of the fluid turbulence, without the need of any dispersion model, thus resulting in more physical and more universal description of the fluid–particle interactions. Quite satisfactory agreement was observed between simulations and experiments considering the complexity of the flow and the difficulties arising from the determination of proper injection conditions for the particles. The overall structure of the mean airflow was fairly well predicted, even if experimental and numer-

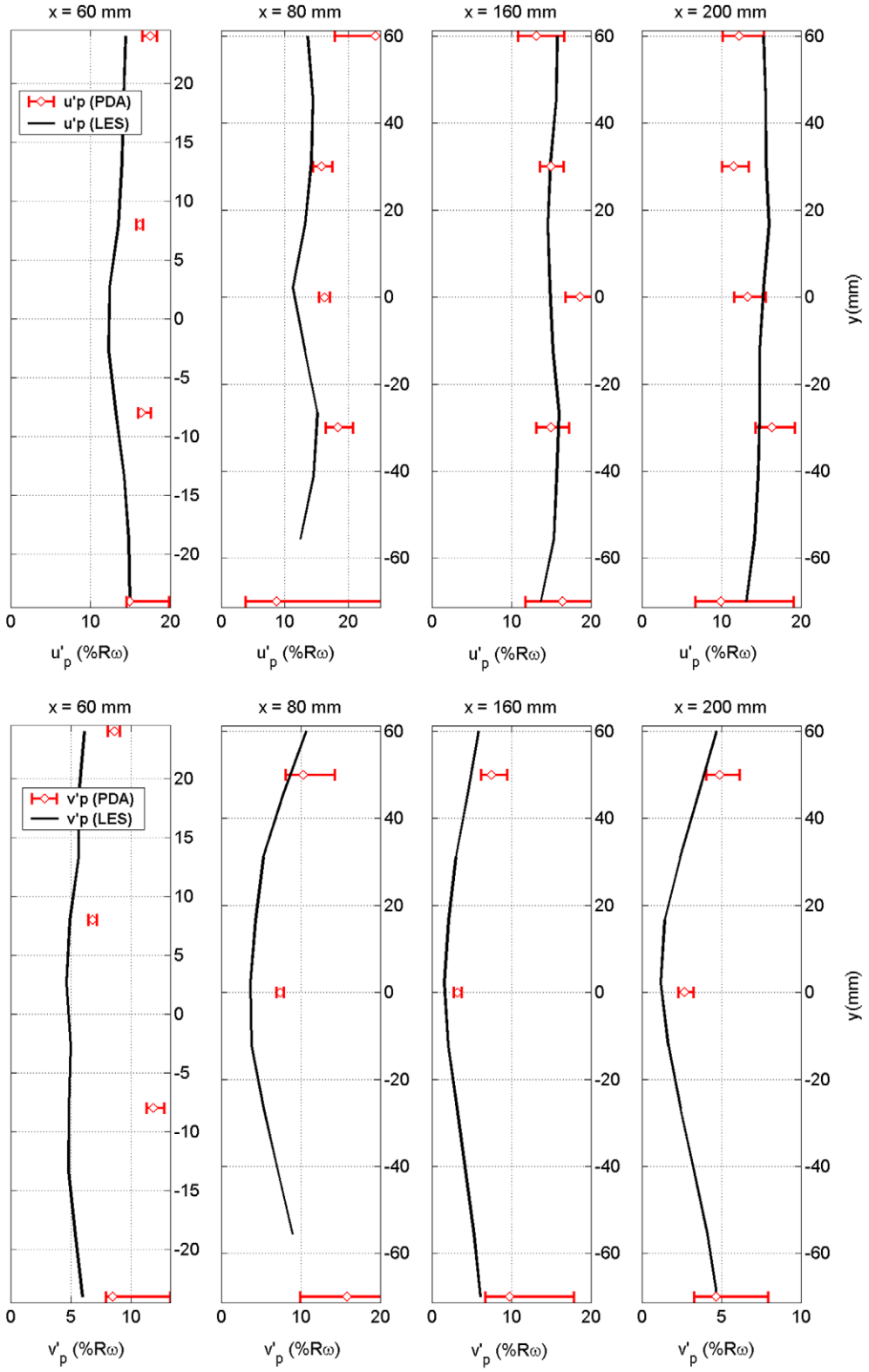

Fig. 14. Profiles of particle fluctuating velocity in the horizontal plane $z = 0$: comparison between PDPA measurements (dashed lines with error bars) and LES computation (solid lines) for the r.m.s. velocity in direction x (top) and in direction y (bottom).

ical results do not match perfectly. It is unclear whether the slight discrepancies between measured and predicted airflows can be attributed to the sole modelling approach, since other phenomena were shown to be possibly influential. Besides the issue of particle initial conditions, direct comparisons were made difficult because of the rapid spatial variations of the flow since small position uncertainties could result in large variations of any considered quantity. Moreover, the measurement error for air velocity was higher in regions of high concentration of particles, especially near the inception of the jet, because of the intricate problem of phase

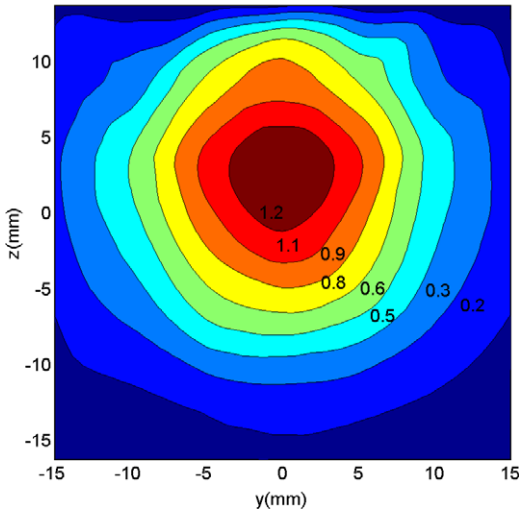

Fig. 15. Contours of measured ratio τ_p/τ_c at $x = 30$ mm ($\omega = 1000$ rpm, $d_p = 100$–200 μm, 49 points-based evaluation).

discrimination. Besides inevitable bias arising from the discrimination algorithm, the high rejection rate of measurements in such zones did not always allow satisfactory statistical convergence. It should also be noticed that the true velocity fluctuations of air remained unavailable for comparisons because PIV provides only filtered fluctuations. It is therefore clear that there was still some lack of experimental data for two-phase cases in the jet source region.

Even if promising results were obtained, closer validation seems to be required for the long-term purpose of our study, especially concerning the turbulence modification by particles: turbulence intensity was found to range typically between 30% and 100% in the test rig, therefore turbulent transport would be the most influent dispersion factor if a passive pollutant were emitted simultaneously with the solid particles. The objective of better validation of particle–turbulence interactions necessarily goes through a better knowledge and modelling of the particle behaviour close to the jet source. We showed that the effect of particle-to-particle collisions is significant in this region and may persist along a noticeable distance. This underlines the main weakness of our simulations since collisions probably play some role in the velocity distributions of particles as well as in the spread rate of the jet. Further work will be devoted to the implementation of inter-particle collisions into the process of Lagrangian trajectory computation using a probabilistic collision model (Oesterlé and Petitjean, 1993; Sommerfeld, 2001). Let us mention finally another aspect requiring further development, namely the possible effect of particles upon the subgrid scales, which was not taken into account here in spite of some possibly noticeable effect due to the locally high mass fraction of particles.

Acknowledgements

This experimental and numerical work was carried in the frame of a collaboration between the French National Institute for Safety and Health (INRS) and the LEMTA laboratory, CNRS, Nancy University. The first author acknowledges the financial support of the National Association for Technical Research (ANRT).

References

Abrahamson, J., 1975. Collision rates of small particles in a vigorously turbulent fluid. Chem. Eng. Sci. 30, 1371–1379.
Andersson, H.I., Lygren, M., 2006. LES of open rotor–stator flow. Int. J. Heat Fluid Flow 27, 551–557.
Bachalo, W.D., 1994. Experimental methods in multiphase flows. Int. J. Multiphase Flow 20, 261–295.
Belut, E., 2006. Etude des écoulements d'air et de particules au voisinage de pièces en mouvement: application à la conception des captages sur machines tournantes réalisant des opérations d'usinage. Ph.D. Thesis, Université Henri Poincaré, Nancy, France.
Belut, E., Bonthoux, F., Bruchhausen, M., Lemoine, F., 2006. Experimental characterisation of a solid particles jet generated by a pseudo machining operation. Proc. VENT 2006 – 8th Int. Conf., Chicago, IL, USA.
Belut, E., Bonthoux, F., Fontaine, J.-R., Kheiri, A., Oesterlé, B., 2005. Comparaison de modèles de turbulence sur le cas du disque tournant. Proc. 17ième Congrès Français de Mécanique, Troyes, France, CD-ROM, #1141.
Bradshaw, P., Terrell, M.C., 1969. The response of a turbulent boundary layer on an infinite swept wing to the sudden removal of pressure gradient. NPL Aero Report 1305, National Physical Laboratories.
Chagras, V., Oesterlé, B., Boulet, P., 2005. On heat transfer in gas–solid pipe flows: effects of collision-induced alterations of the flow dynamics. Int. J. Heat Mass Transfer 48, 1649–1661.
Christensen, K.T., 2004. The influence of peak-locking errors on turbulence statistics computed from PIV ensembles. Exp. Fluids 36, 484–497.
Crowe, C.T., Sommerfeld, M., Tsuji, Y., 1998. Multiphase Flows with Droplets and Particles. CRC Press, Boca Raton.
Fukagata, K., 2000. Large eddy simulation of particulate turbulent channel flows. Report S-100 44, Kungl. Tekniska Högskolan – Faxén Laboratoriet, Stockholm, Sweden.
Kim, W.W., 2004. Large eddy simulation using unstructured meshes and dynamic subgrid-scale turbulence models. In: Proceedings of the 34th Fluid Dynamics Conference and Exhibit, Portland, OR, USA. #AIAA-2004-2548.
Kim, W.W., Menon, S., 1997. Application of the localized dynamic subgrid-scale model to turbulent wall-bounded flows. In: Proceedings of the 35th Aerospace Sciences Meeting, Reno, NV, USA. #AIAA-97-0210.
Kulick, J.D., Fessler, J.R., Eaton, J.K., 1994. Particle response and turbulence modification in a fully developed channel flow. J. Fluid Mech. 277, 109–134.
Littell, H.S., Eaton, J.K., 1994. Turbulence characteristics of the boundary layer on a rotating disk. J. Fluid Mech. 266, 175–207.
Morsi, S.A., Alexander, A.J., 1972. An investigation of particle trajectories in two-phase flow systems. J. Fluid Mech. 55, 193–208.
Oesterlé, B., Petitjean, A., 1993. Simulation of particle-to-particle interactions in gas–solid flows. Int. J. Multiphase Flow 19, 199–211.
Okamoto, K., Nishio, S., Saga, T., Kobayashi, T., 2000. Standard images for particle-image velocimetry. Meas. Sci. Technol. 11, 685–691.
Piomelli, U., 2004. Large-eddy and direct simulation of turbulent flows. Von Karman Institute for Fluid Dynamics – Lecture Series, 2004–2006.
Shih, T.H., Liou, W.W., Shabbir, A., Yang, Z., Zhu, J., 1995. A new k—ε eddy-viscosity model for high Reynolds number turbulent flows – model development and validation. Comput. Fluids 24, 227–238.
Sommerfeld, M., 1995. The importance of inter-particle collisions in horizontal gas–solid channel flows. In: Proceedings of the 6th International Symposium on Gas–Solid Flows, ASME-FED 228, pp. 335–345.
Sommerfeld, M., 2001. Validation of a stochastic Lagrangian modelling approach for inter-particle collisions in homogeneous isotropic turbulence. Int. J. Multiphase Flow 27, 1829–1858.
Stanislas, M., Okamoto, K., Kaehler, C., 2003. Main results of the first international PIV challenge. Meas. Sci. Technol. 14, R63–R89.
Tanaka, T., Tsuji, Y., 1991. Numerical simulation of gas–solid two-phase flow in a vertical pipe: on the effect of inter-particle collisions. In: Proceedings of the 4th International Symposium on Gas–Solid Flows, ASME-FED, vol. 121, pp. 123–128.
Theodorsen, T., Regier, A., 1944. Experiments on drag of revolving disks, cylinders, and streamline rods at high speed. NACA Report 793.
Thomas, M., Misra, S., Kambhamettu, C., Kirby, J.T., 2005. A robust motion estimation algorithm for PIV. Meas. Sci. Technol. 16, 865–877.
Yamamoto, Y., Potthoff, M., Tanaka, T., Kajishima, T., Tsuji, Y., 2001. Large-eddy simulation of turbulent gas–particle flow in a vertical channel: effect of considering inter-particle collisions. J. Fluid Mech. 442, 303–334.